Channel Density Regulation of Firing Patterns in a Cortical Neuron Model

P. Århem,* G. Klement,* and C. Blomberg†
*Nobel Institute for Neurophysiology, Department of Neuroscience, Karolinska Institutet, SE-17177 Stockholm, Sweden; and †Department of Physics, KTH-Albanova, SE-62016 Stockholm, Sweden

ABSTRACT Modifying the density and distribution of ion channels in a neuron (by natural up- and downregulation or by pharmacological intervention or by spontaneous mutations) changes its activity pattern. In this investigation we analyzed how the impulse patterns are regulated by the density of voltage-gated channels in a neuron model based on voltage-clamp measurements of hippocampal interneurons. At least three distinct oscillatory patterns, associated with three distinct regions in the Na-K channel density plane, were found. A stability analysis showed that the different regions are characterized by saddle-node, double-orbit, and Hopf-bifurcation threshold dynamics, respectively. Single, strongly graded action potentials occur in an area outside the oscillatory regions, but less graded action potentials occur together with repetitive firing over a considerable range of channel densities. The relationship found here between channel densities and oscillatory behavior may partly explain the difference between the principal spiking patterns previously described for crab axons (class 1 and 2) and cortical neurons (regular firing and fast spiking).

INTRODUCTION

Electric brain activity is characterized by oscillatory patterns caused by dynamically interacting neuronal groups. The determinants of these patterns, and thus of associated perceptual and behavioral states, include the configuration of the neural network, the strength and type of the synaptic connections, and the intrinsic firing/resonance properties of the neurons (1). Factors determining the intrinsic firing properties include dendritic morphology (2) and composition of ion channel mixture (see Hille (3)). An increasing number of studies show that the ion channel density and distribution vary continuously during normal activity, either to maintain or to modify the firing patterns in a fluctuating firing environment (4,5). Likewise, drugs as general anesthetics and antiepileptics function by selectively blocking or activating channels (6,7), thereby modifying the interacting patterns. Our aim here is to analyze how the density of a class of ion channels, the voltage-gated ones, regulates the impulse-firing patterns by studying a simple neuron model.

The model neuron is based on a voltage clamp analysis of a subgroup of hippocampal interneurons. This group shows stimulus-dependent action potentials (8,9), thus deviating from the received view that most neurons follow the all-or-nothing law (10). Numerical calculations, based on the Hodgkin-Huxley formalism, suggest that the graded behavior in these cells is mainly due to low Na channel density. When we increased the density in the model calculations, all-or-nothing behavior and repetitive firing appeared. Graded behavior has also been demonstrated in the classical squid axon preparation when temperature is increased to room temperature (11), suggesting that graded behavior is more common in central neurons than previously recognized. The model neuron thus allows us to analyze not only the channel density-dependent oscillatory activity but also its relationship with the gradedness of the impulses.

In contrast to other cases reported, where the mathematical descriptions can be reduced to simpler systems (FitzHugh-Nagumo and Morris-Lecar models), the model in this study was not readily simplified to a two-dimensional system. We therefore used the full set of differential equations and analyzed the stability of the stationary solutions. The analysis revealed that the oscillatory activity could be classified in at least three distinct patterns associated with three distinct regions in the channel density plane. The different oscillatory regions are associated with different action potential threshold behaviors, one region showing a discontinuous current threshold and the others a zone of steeply, although continuously, increasing voltage amplitude. The capacity for gradedness shows a complex relation to the capacity for repetitive firing; strongly graded action potentials occur in an area of the channel density plane outside oscillatory regions, but less graded action potentials occur together with repetitive firing over a considerable range of K and Na channel densities.

The relationship found between channel densities and oscillatory behavior explains the difference between the principal spiking patterns previously described for crab axons and cortical neurons; the spike pattern of Hodgkin's class 1 axons and regular spiking pyramidal cells on one side and that of class 2 axons and fast spiking interneurons on the other side (12,13). The relationships found explain reported impulse pattern modifications in cells at selective channel blockade (14), and open up for novel explanations of pattern modifications in the brain, caused by selective up- and downregulation of channels or by action of general anesthetics. The latter fact also makes the relationships found

Submitted November 2, 2005, and accepted for publication February 14, 2006.

Address reprint requests to Peter Århem, Nobel Institute for Neurophysiology, Dept. of Neuroscience, Karolinska Institutet, SE-17177 Stockholm, Sweden. E-mail: peter.arhem@ki.se.

0006-3495/06/06/4392/13 $2.00

doi: 10.1529/biophysj.105.077032

suggest a possible strategy for constructing novel general anesthetics.

ANALYSIS

The model

For this analysis, we use a neuron model based on recordings from small sized hippocampal interneurons at room temperature (3,4). The mathematical description follows that of Frankenhaeuser and Huxley (15), which differs slightly from the classical Hodgkin-Huxley description (16) in using i) the permeability concept rather than the conductance concept (17), ii) other kinetic equations (m^2 instead of m^3 and n^2 instead of n^4), and iii) other values for the rate functions. The reason for the difference between the kinetics of the two axon types is possibly a species difference: the Frankenhaeuser-Huxley description applies to vertebrate myelinated axons and the Hodgkin-Huxley description to molluscan giant axons.

The basic equations are

$$\begin{aligned} dv/dt &= I(v,m,h,n)/C_{\mathrm{M}} \\ &= (I_{\mathrm{S}} - I_{\mathrm{Na}}(v,m,h) - I_{\mathrm{K}}(v,n) - I_{\mathrm{L}}(v))/C_{\mathrm{M}} \end{aligned} \quad (1)$$

$$dm/dt = \alpha_{\mathrm{m}}(v)\times(1-m) - \beta_{\mathrm{m}}m \quad (2)$$

$$dh/dt = \alpha_{\mathrm{h}}(v)\times(1-h) - \beta_{\mathrm{h}}h \quad (3)$$

$$dn/dt = \alpha_{\mathrm{n}}(v)\times(1-n) - \beta_{\mathrm{n}}n, \quad (4)$$

where v is membrane voltage, m and h are variables describing the fraction of activated (m) and inactivated ($1-h$) Na channels, and n is a variable describing the fraction of activated K channels. I_{s} the stimulation current and

$$\begin{aligned} I_{\mathrm{Na}} = A_{\mathrm{M}}P_{\mathrm{Na}}\times(vF^2/RT)\times([Na]_{\mathrm{o}} - [Na]_{\mathrm{I}} \\ \times exp(vF/RT))/(1-exp(vF/RT)) \end{aligned} \quad (5)$$

is the current through Na channels, where A_{M} denotes the membrane area, and F, R, and T have their normal thermodynamic meanings. $[Na]_{\mathrm{o}}$ and $[Na]_{\mathrm{i}}$ denote extracellular and intracellular Na concentrations, respectively.

$$\begin{aligned} I_{\mathrm{K}} = A_{\mathrm{M}}P_{\mathrm{K}}\times(vF^2/RT)\times([K]_{\mathrm{o}} - [K]_{\mathrm{I}} \\ \times exp(vF/RT))/(1-exp(vF/RT)) \end{aligned} \quad (6)$$

is the current through K channels and

$$I_{\mathrm{L}} = (v - V_{\mathrm{R}})/R_{\mathrm{M}} \quad (7)$$

is the current through leak channels. V_{R} is resting potential and R_{M} the leak resistance.

$$P_{\mathrm{Na}} = P^*_{\mathrm{Na}} \times hm^2 \quad (8)$$

is the Na channel permeability and P^*_{Na} the permeability value when all Na channels are open, i.e., when $h = m = 1$.

$$P_{\mathrm{K}} = P^*_{\mathrm{K}} \times n^2 \quad (9)$$

represents in the same way the K channel permeability. The P^*_{Na} and P^*_{K} values are proportional to the Na and K channel densities in the cell membrane (number of channels per membrane area).

The rate functions for Eqs. 2–4 are

$$\begin{aligned} \alpha_{\mathrm{m}} = A_{\alpha\mathrm{m}}\times((v - V_{\mathrm{R}}) - B_{\alpha\mathrm{m}})/ \\ (1 - exp\{[B_{\alpha\mathrm{m}} - (v - V_{\mathrm{R}})]/C_{\alpha\mathrm{m}}\}) \end{aligned} \quad (10)$$

$$\begin{aligned} \beta_{\mathrm{m}} = A_{\beta\mathrm{m}}\times(B_{\beta\mathrm{m}} - (v - V_{\mathrm{R}}))/ \\ (1 - exp\{[((v - V_{\mathrm{R}}) - B_{\beta\mathrm{m}}]/C_{\beta\mathrm{m}}\}) \end{aligned} \quad (11)$$

$$\begin{aligned} \alpha_{\mathrm{h}} = A_{\alpha\mathrm{h}}\times(B_{\alpha\mathrm{h}} - (v - V_{\mathrm{R}}))/ \\ (1 - exp\{[(v - V_{\mathrm{R}}) - B_{\alpha\mathrm{h}}]/C_{\alpha\mathrm{h}}\}) \end{aligned} \quad (12)$$

$$\beta_{\mathrm{h}} = A_{\beta\mathrm{h}}/(1 + exp\{[B_{\beta\mathrm{h}} - (v - V_{\mathrm{R}})]/C_{\beta\mathrm{h}}\}) \quad (13)$$

$$\alpha_{\mathrm{n}} = A_{\alpha\mathrm{n}}((v - V_{\mathrm{R}}) - B_{\alpha\mathrm{n}})/(1 - exp\{[B_{\alpha\mathrm{n}} - (v - V_{\mathrm{R}})]/C_{\alpha\mathrm{n}}\}) \quad (14)$$

$$\beta_{\mathrm{n}} = A_{\beta\mathrm{n}}(B_{\beta\mathrm{n}} - (v - V_{\mathrm{R}}))/(1 - exp\{[(v - V_{\mathrm{R}}) - B_{\beta\mathrm{n}}]/C_{\beta\mathrm{n}}\}), \quad (15)$$

with constants A, B, and C listed in Table 2. Values of the other constants used are summarized in Table 1.

The differential equations were solved by numerical integration (Runge-Kutta methods). The initial conditions used were $v = V_{\mathrm{R}}$, $n = m = 0$, $h = 1$. The channel densities were changed by changing the value of the permeability parameters P^*_{Na} and P^*_{K}, whereas the kinetic and the passive membrane parameters were kept constant. In model terms, this means that the calculations describe the time evolution of the membrane voltage in a neuron with a constant and simple (single compartment) morphology and with two homogenously distributed ion channel populations (Na and delayed rectifier K channels) of variable density.

Features of the model: gradedness and oscillatory behavior

Fig. 1 illustrates some activity features of the model. The responses to sub- and suprathreshold current pulses of the original or default model (i.e., with $P^*_{\mathrm{Na}} = 1.3 \times 10^{-6}$ and $P^*_{\mathrm{K}} = 0.24 \times 10^{-6}$ m s^{-1}) are shown in the upper panel (*A*), the responses of a model with an increased Na channel but retained low K channel density ($P^*_{\mathrm{Na}} = 30 \times 10^{-6}$ and $P^*_{\mathrm{K}} = 0.24 \times 10^{-6}$ m s^{-1}) is shown in the middle (*B*), and the responses of a model with both Na and K channel densities increased 20-fold ($P^*_{\mathrm{Na}} = 26 \times 10^{-6}$ and $P^*_{\mathrm{K}} = 4.8 \times 10^{-6}$ m s^{-1}) are shown in the lower panel (*C*). The subthreshold responses in all cases reflect the unchanged, relatively long time constant of the passive membrane (30 ms = 7 pF × 4.3 GΩ). Single action potentials are elicited in the low channel density case (Fig. 1 *A*) and in the high Na/low K channel density case (Fig. 1 *B*), whereas repetitive action potentials is seen in the high density case (Fig. 1 *C*). The action potential amplitude increases with stimulation in all cases but clearly most in the low density case (1.7-fold between the impulses

TABLE 1 Values of parameters used in the equations

V_R	resting potential (−70 mV)
P^*_{Na}	permeability for Na^+ when all Na channels are open (default value 1.3×10^{-6} m s^{-1})
P^*_K	permeability for K^+ when all K channels are open (default value 0.24×10^{-6} m s^{-1})
A, B, C	empirical constants for α and β given in Table 2
A_M	membrane area (10^{-4} m^{-2})
R	gas constant (8.3143 J K^{-1} mol^{-1})
F	Faraday's constant (9.64870 10^4 C mol^{-1})
T	absolute temperature (280 K)
C_M	membrane capacitance (7 pF)
R_M	leak resistance (4.3GΩ)
$[Na]_i$, $[Na]_o$	Na^+ concentration in intracellular and extracellular solution (14 and 114.5 mol m^{-3})
$[K]_i$, $[K]_o$	K^+ concentration in intracellular and extracellular solution (120 and 2.5 mol m^{-3})

at 10 and 40 pA) and least in the high Na/low K channel density case (~4%). This reflects the general trend that the amplitude sensitivity decreases with increased P^*_{Na} and decreased P^*_K, converging toward all-or-nothing behavior at $P^*_{Na} > 30 \times 10^{-6}$ m s^{-1} and $P^*_K < 0.24 \times 10^{-6}$ m s^{-1}. This density-dependent switch between the capacity for producing stimulus-dependent single action potentials and for producing repetitive firing suggests that neuronal information processing may switch from amplitude code to rate code by channel up- or downregulation.

Fig. 2 shows the firing behavior of the model with three different channel density combinations at increasing stimulation amplitudes. In all three cases the stimulation elicits repetitive firing at some interval, and in all three cases the firing terminates as damped oscillations. The three cases represent different dynamics. In case A ($P^*_{Na} = 20 \times 10^{-6}$ and $P^*_K = 20 \times 10^{-6}$ m s^{-1}) sustained oscillatory activity appears as an infinite prolongation of damped oscillations with a frequency ~16 Hz, whereas it disappears abruptly at a frequency of 120 Hz. Case B ($P^*_{Na} = 20 \times 10^{-6}$ and $P^*_K = 10 \times 10^{-6}$ m s^{-1}) shows similar dynamics at threshold but terminates continuously as the amplitude approaches zero. In case C ($P^*_{Na} = 20 \times 10^{-6}$ and $P^*_K = 5 \times 10^{-6}$ m s^{-1}) oscillatory activity emerges with very low frequency unlike case A and B, whereas it terminates like case B, i.e., continuously.

Fig. 3 shows how the oscillatory activity of the model relates to the P^*_{Na}-P^*_K plane (or Na-K channel density plane) at different stimulations (5–80 pA). The area within each contour represents permeability (or density) pairs that provide oscillations in the model at the given stimulation strength.

Stability analysis

To analyze the nature of the oscillations and the excitability of the model neuron, we performed a standard stability analysis of the full set of differential equations. Often, one reduces such a system by assigning certain relations between the main quantities (as is done in, e.g., the FitzHugh-Nagumo and Morris-Lecar models (18)), which leads to a simpler geometric analysis of the solutions. Although such a reduced model undoubtedly has some advantages by providing more illustrative results, we found that many important features were not reproduced appropriately and, therefore, we refrained from such reductions.

As a starting point in the stability analysis, we calculate and characterize the stationary states of Eqs. 1–4 for which all time derivatives are zero. The right hand sides of Eqs. 1–4 are then equal to zero. With $j = m$, h, or n, we write

$$j_\infty(v) = \alpha_j(v)/(\alpha,(v) + \beta_j(v)). \quad (16)$$

The time derivatives of m, h, and n are zero when

$$m = m_\infty(v); h = h_\infty(v); n = n_\infty(v). \quad (17)$$

We put these expressions into Eq. 1 and find that $dv/dt = 0$ when

$$I_\infty(v) = I(v, m_\infty(v), h_\infty(v), n_\infty(v)) = 0. \quad (18)$$

Equation 18 provides a single equation for a stationary potential, v, and can be solved numerically. We write such a stationary solution as $v = v0$. The other parameters then get stationary values:

$$m = m_0 = m_\infty(v0), h = h_0 = h_\infty(v0), n = n_0 = n_\infty(v0). \quad (19)$$

Next, we investigate the character of this stationary solution when the stimulation current, I_s, and the permeability parameters, P^*_{Na} and P^*_K, are varied. This is done in a standard way by linearizing the right-hand sides of Eqs. 1–4 close to the stationary states. The details of this procedure are described in the Appendix. The main characterizing quantity is a 4×4 matrix, JM, the values of which are given as partial derivatives of the right-hand side expressions in Eqs. 1–4 with respect to the four variables (v, m, h, n) and calculated at

TABLE 2 Values of *A*, *B*, and *C* in Eqs. 10–15

	α_h	β_h	α_m	β_m	α_n	β_n
A ($s^{-1}V^{-1}$)	50×10^3	2.25×10^6 *	60×10^3	60×10^3	16×10^3	16×10^3
B (V)	5×10^{-3}	60×10^{-3}	37×10^{-3}	28×10^{-3}	60×10^{-3}	35×10^{-3}
C (V)	6×10^{-3}	10×10^{-3}	3×10^{-3}	20×10^{-3}	10×10^{-3}	10×10^{-3}

*(s^{-1}).

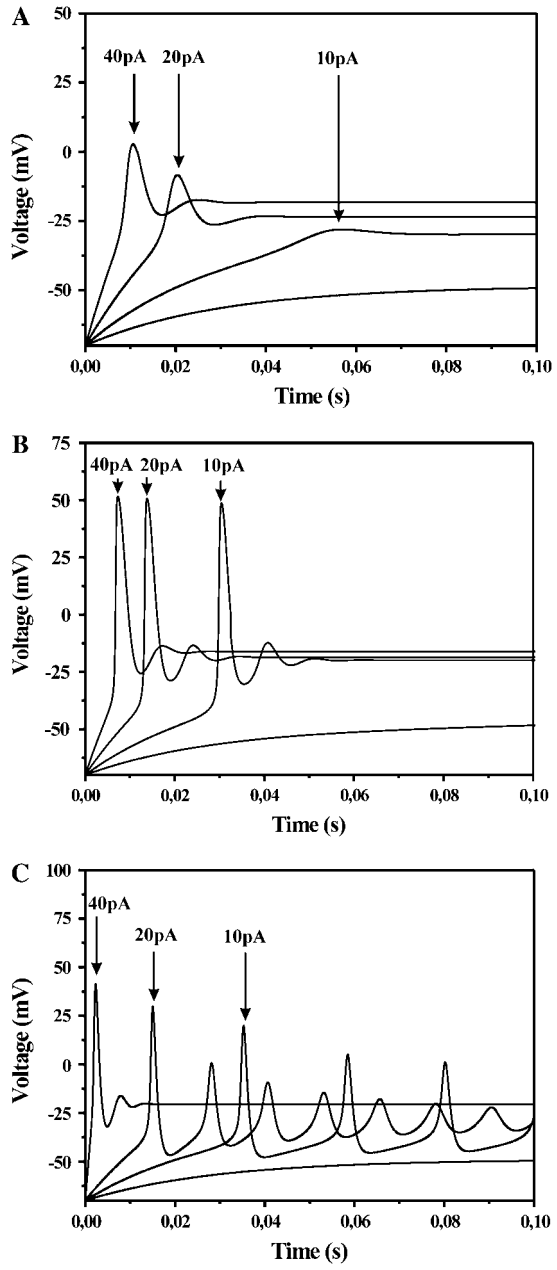

FIGURE 1 Features of the neuron model. Computed action potentials at different channel densities, demonstrating density-dependent changes in gradedness and oscillatory behavior. The low density case (*A*), $P^*_{Na} = 1.3 \times 10^{-6}$ and $P^*_K = 0.24 \times 10^{-6}$ m s^{-1}, shows high sensitivity (graded amplitude), the high Na/low K channel density case (*B*), $P^*_{Na} = 30 \times 10^{-6}$ and $P^*_K = 0.24 \times 10^{-6}$ m s^{-1}, shows low sensitivity (all-or-nothing-like behavior) and the high density case (*C*), $P^*_{Na} = 26 \times 10^{-6}$ and $P^*_K = 4.8 \times 10^{-6}$ m s^{-1}, shows repetitive firing. Applied current was 5, 10, 20, and 40 pA.

an appropriate stationary state with parameter values as shown above. The character of the stationary state is determined by the four eigenvalues of the matrix *JM*. Two eigenvalues are always real and negative. The remaining two thus determine the stability of the system. For sufficiently low stimulation currents or low values of any of the P^*-parameters (the density of the channels), all four eigenvalues are real and negative. Then, the system reaches a stable state from any initial state (see Table 5 in the Appendix). In some cases, one eigenvalue is positive, whereas all others are negative, which yields saddle-point behavior. In all other cases, and that covers the more interesting behaviors, two eigenvalues are complex with positive or negative real parts. If the real parts are positive, the stationary state is unstable. In all investigated situations, this leads to sustained oscillations. If the real parts are negative, the stationary state is stable. This does not mean, however, that all trajectories approach this stable state. There are situations when, depending on the initial conditions, trajectories lead to sustained oscillations around the stable state. Such a situation cannot be analyzed in any simple way.

The fact that there are always two real, negative eigenvalues of the *JM* matrix, which never show large variations, indicates that the essential variation of the four variables takes place on a two-dimensional surface in the four-dimensional variable space. This may motivate a reduction of the variables, but the surface is not simple and not describable in simple analytic terms. Still, it suggests that relevant parts of the dynamics are of a two-dimensional character, from which certain conclusions can be made. In particular, this would exclude further complex types of solutions, such as irregular, ''chaotic'' solutions or oscillations with two separate frequencies.

Oscillations for a point in the P^*_{Na}-P^*_K plane appear when the value of the stimulation current I_S lies within a certain interval. The onset of oscillations at the lower limit of this stimulation interval and the cessation at the upper limit appear in three ways. Either they appear i), via a ''conventional Hopf-bifurcation'', that is the positive part of the complex eigenvalues of the matrix *JM* changes sign; or they appear ii), via a ''double-orbit bifurcation'', meaning that a pair of periodic orbits appears around a stable, stationary point, one being unstable with a separating role and the other being stable. The latter yields sustained oscillations for initial conditions outside a manifold that contains the unstable orbit (see Fig. 4). Or, finally, they appear iii), via a ''saddle-node bifurcation'', meaning that there are three stationary states, where two (one stable node and one saddle point) go together and vanish, leaving one unstable state, which yields sustained oscillations.

Three distinct oscillatory activity regions in the channel-density plane

With the stability analysis as a basis, we can provide a more specific characterization of the model activity for different values of the P^*_{Na} and P^*_K parameters, i.e., for different points in the Na-channel–K-channel density plane. This analysis distinguishes three distinct regions in the density plane.

Region A: This region (represented by the case of Fig. 2 *A*) comprises relatively low P^*_{Na} values and high P^*_K values,

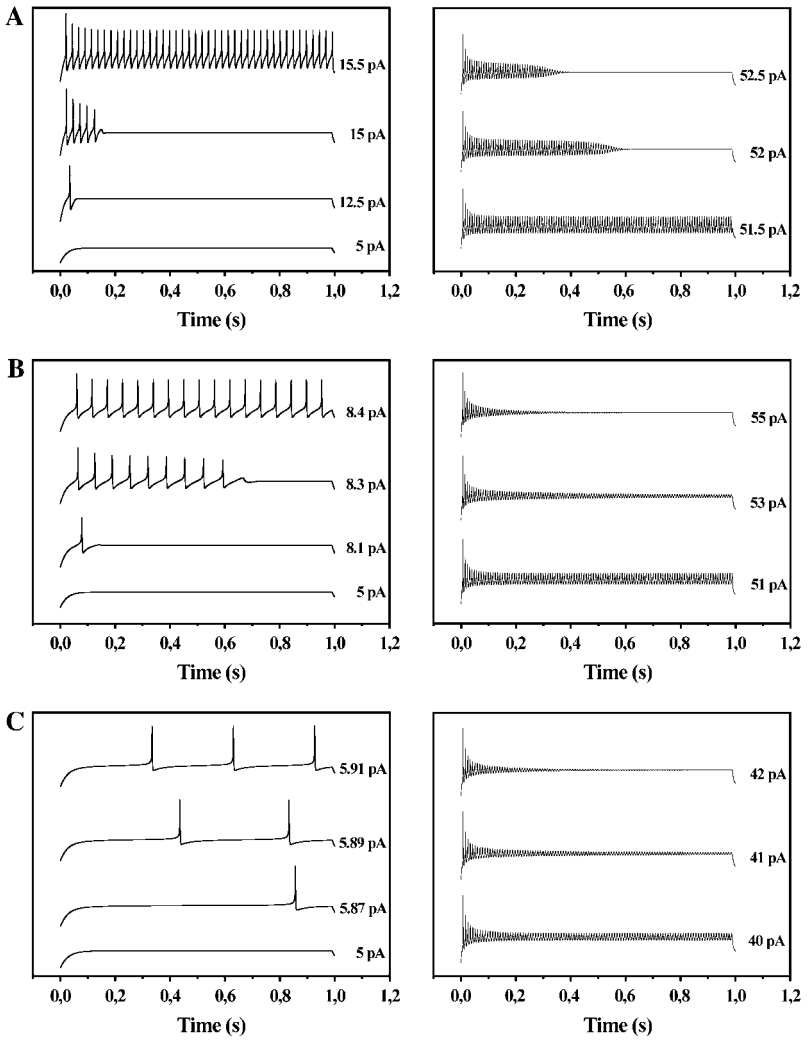

FIGURE 2 Responses of the neuron model to increased stimulation current at different channel densities, demonstrating different onset (*left*) and termination (*right*) patterns of the oscillations. The high density case (*A*), with permeability values $P^*_{Na} = 20 \times 10^{-6}$ and $P^*_K = 20 \times 10^{-6}$ m s^{-1}, displays an abrupt onset and abrupt termination, case (*B*) with permeability values $P^*_{Na} = 20 \times 10^{-6}$ and $P^*_K = 10 \times 10^{-6}$ m s^{-1}, displays an abrupt onset and a continuous amplitude decrease at termination and case (*C*), with permeability values $P^*_{Na} = 20 \times 10^{-6}$ and $P^*_K = 5 \times 10^{-6}$ m s^{-1}, displays a continuous onset and a continuous amplitude decrease at termination.

for which the solution to Eq. 18 is unambiguous and stable and all eigenvalues of the *JM* matrix are negative or complex with negative real parts. This means that a solution trajectory always reaches the stationary value if it starts at initial conditions sufficiently close to it. However, as mentioned above, this does not exclude oscillations, and we distinguish two parts of the A region: A1 (the lowest P^*_{Na}-values), where oscillations never occur, and a region A2, where oscillations appear for each point (each P^*_{Na}-P^*_K pair) via a double-orbit bifurcation within some interval of the stimulation current. This means that two orbits, representing periodic behavior, appear simultaneously in the variable space and then go away from each other. One of the orbits yields stable, sustained oscillations. A trajectory in the *n*-*v* plane that demonstrates this double-orbit appearance is shown in Fig. 4.

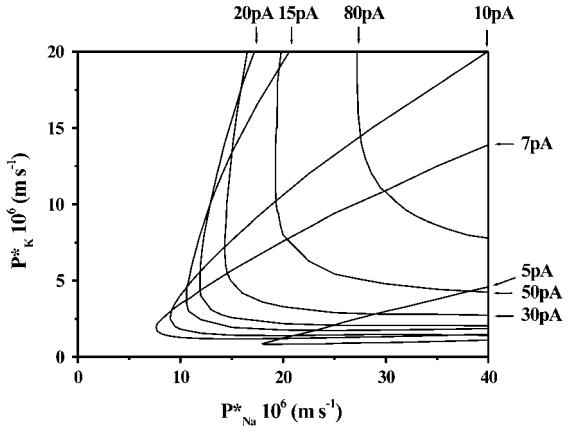

FIGURE 3 Regions in the P^*_{Na}-P^*_K plane showing where the neuron model fires repetitively at the stimulation currents indicated.

Region B: This region (represented by the case of Fig. 2 *B*) is also characterized by always having an unambiguous solution to Eq. 18. In this case, however, the solution is unstable within a certain stimulation interval as the eigenvalues are complex with positive real parts, which necessarily leads to oscillations via a Hopf-bifurcation. The situation is complicated, since oscillations around stable stationary states also occur, similar to the situation of region A2. We will later consider certain implications for the onset and cessation of the oscillations.

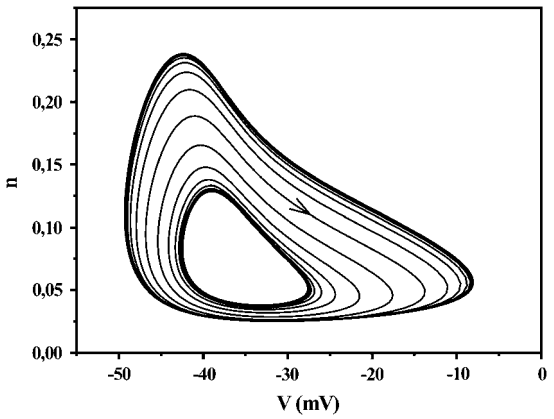

FIGURE 4 Double-orbit bifurcation dynamics. Projection of a trajectory on the n-v plane of a region A2 neuron model stimulated by 18 pA. The trajectory starts at the inner unstable orbit and moves clockwise toward the outer stable orbit. Model permeability values are $P^*_{Na} = 14 \times 10^{-6}$ and $P^*_K = 10 \times 10^{-6}$ m s^{-1}.

Region C: In contrast to the situation for all points in regions A and B, where I_∞ (Eq. 18) is monotonously decreasing with potential v, I_∞ for points in region C (represented by the case of Fig. 2 *C*) increases within a certain potential range. The consequence of this fact is that within a certain stimulation interval (up to ~5–7 pA), Eq. 18 yields three solutions, i.e., three possible stationary states. The one with the lowest potential value always provides a stable state, a ''node'' (the eigenvalues are all real and negative). An intermediate potential value corresponds to a saddle point, which, together with trajectories leading to that state, separates regions of different character. With the initial state used in this study ($v = -70$ mV), solution trajectories always target the stable state with lowest potential in a direct manner, without any extra pulse or damped oscillations. When the stimulation current increases, the two stationary points at the lowest potential values merge and vanish, leaving the solution with the largest potential value as the only stationary point available. This high potential stationary point is not reached at lower stimulations from our initial conditions but discontinuously takes over at the bifurcation (when the stable point and the saddle node merge). Depending on the stability criterion, we can distinguish two regions associated with different oscillation patterns: C1 with higher P^*_K values, where this high potential stationary state is unstable within a stimulation interval (the eigenvalues being complex with positive real parts) and thus leads to oscillatory behavior of the model neuron via a saddle-node bifurcation, or C2 with lower P^*_K values, where the high potential stationary state is always stable.

In summary, the channel density plane can be separated into three distinct regions (A, B, and C; represented by the cases of Fig. 2, *A–C*, respectively), characterized by the solutions to Eq. 18 (Fig. 5). The region in the density plane yielding oscillatory activity for some stimulation interval comprises the subregions A2, B, and C1. As we will discuss later, solutions in the form of pulses appear differently for points in region A1 than for nonoscillating solutions in other regions. The oscillatory behavior looks essentially the same for points in the oscillating regions. However, the onset and cessation of the oscillations differ due to different kinds of bifurcation scenarios.

The double-orbit bifurcations occur at the lower limit of the stimulation interval for region A2 neuron models and at the upper limit for region A2 and B neuron models. At the lower limit the oscillations start with nonzero amplitude and frequency (when the two orbits appear or vanish) and at the upper limit they cease abruptly with nonzero amplitude and frequency. Double-orbit behavior should be possible to establish empirically by investigating the sensitivity to initial conditions. It shows hysteresis if the stimulation current is slowly changed through a bifurcation point, i.e., an increase or decrease of the stimulation could lead to different results. The Hopf-bifurcations occur at the lower limit of the stimulation interval for region B neuron models and at the upper limit in region B and C1 neuron models. At the lower stimulation interval limit, the oscillations start abruptly with nonzero frequency and nonzero amplitude, whereas at the upper limit the oscillations cease when the amplitude reaches zero (at a nonzero frequency). The saddle-node bifurcations, finally, occur only at the onset of oscillations for region C1 neuron models and means that oscillations start with a very low (zero) frequency and nonzero amplitude. The discussed features are summarized in Table 3.

Boundaries of the oscillatory subregions

The boundaries between the regions A2 and B, between B and C1, and between C1 and C2 can be expressed by analytic expressions, whereas the boundary between A1 and A2 cannot be expressed in any simple way. Region B is characterized

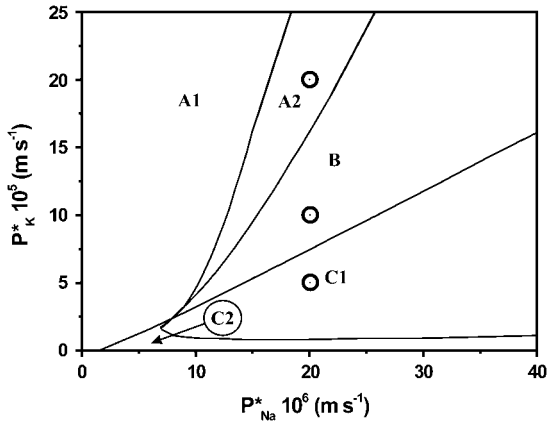

FIGURE 5 Bifurcation map. Regions in the P^*_{Na}-P^*_K plane associated with oscillatory activity of double-orbit (*A2*), Hopf (*B*), and saddle-node (*C1*) bifurcation behavior of the neuron model at some stimulation interval. The oscillatory region is the envelope of all the oscillatory regions in Fig. 3.

TABLE 3 Oscillatory subregions

Region	onset bifurcation limits	End bifurcation limits
A2	Double orbit, $f > 0$, $A > 0$	Double orbit, $f > 0$, $A > 0$
B	Hopf, $f > 0$, $A > 0$	Double orbit, $f > 0$, $A > 0$ Hopf, $f > 0$, $A = 0$
C1	Saddle node, $f = 0$, $A > 0$	Hopf, $f > 0$, $A = 0$

f denotes frequency and A amplitude.

by Hopf-bifurcations at the lower limit of the stimulation intervals, which means that the real parts of the eigenvalues of the linearization matrix JM are changing sign. This matrix is presented in some detail in the Appendix. At the bifurcation point, two eigenvalues are entirely imaginary. We can get a relation for that by equation $P(v) = 0$, where $P(v)$ is a function based on the elements of JM, as discussed in the Appendix (Eq. A12). With the stimulation current I_s as parameter, this leads to a family of curves in the P^*_{Na}-P^*_K diagram, similar to those of Fig. 3, and the boundary of regions A2 and B is the envelope of these curves. The actual form of the envelope is obtained if we require that also the v-derivative of $P(v)$ shall be zero, i.e., $P(v) = 0$ and $dP(v)/dv = 0$. The boundary between regions A and C always involve stable, simple solutions that turn directly toward a stable final point. The boundary of region C1 is given by the limit of possibilities of three solutions of Eq. 18, $I_\infty(v) = 0$. This limit occurs when $I_\infty(v)$ has a horizontal inflection point, expressed by the existence of a common solution to $dI_\infty(v)/dv = 0$ and $d^2I_\infty(v)/dv^2 = 0$.

Encoding functions reflect the different oscillatory patterns

Fig. 6 shows how features of the model neuron pulse trains relate to the stimulation current for various P^*_{Na} and P^*_K values. Fig. 6 *A* shows the frequency of sustained oscillations versus stimulation, the relation most often considered as the principal encoding function. The curves shown were chosen to represent P^*_{Na}-P^*_K pairs in the three oscillatory subregions (A2, B, and C). As seen, all curves show essentially a monotonous increase of frequency with stimulation. (An exception is curve 28/20, displaying a slight drop at the upper end.) They are located close to each other, with the curves representing points in the P^*_{Na}-P^*_K plane with the same P^*_{Na}/P^*_K quotient being most closely located (not shown). Curves with the same P^*_{Na}/P^*_K quotient show great similarities in their initial phases (can be superimposed) but extend differently in their later phases; the higher the P^*_{Na} and P^*_K values, the wider the frequency range. As also seen in Fig. 6 *A*, the curve representing a point in the C1-region (26/4.8), and thus a saddle-node bifurcation, starts with a very low (essentially zero) frequency, whereas the other curves start from nonzero frequencies (see Table 3). In contrast, the amplitude function (Fig. 6 *B*) shows more dispersed curves. They all have a similar shape: starting with a relatively high value they first increase steeply, pass a maximum, and then decrease almost linearly until they drop. The curves representing points in the P^*_{Na}-P^*_K plane where the oscillations cease with a Hopf-bifurcation (i.e., points in the C1 and in part of the B regions; 26/4.8 and 20/10) continue to zero amplitude (at the end very steeply), whereas those representing double-orbit bifurcations (i.e., associated with points in part of the B and in the A2 region; 28/20 and 20/20) end abruptly without reaching zero amplitude (see Table 3).

Initial pulses and amplitude gradedness

With relevant fixed initial conditions (meaning resting conditions) and with relatively low channel densities, the neuron model shows an initial pulse at suprathreshold stimulation in the variable parameter space represented by a trajectory around a stationary state. The amplitude of this initial pulse is always larger than any following pulse. There are no particular features of the initial pulse that reveal whether it is followed by sustained oscillations or an approach to a stable stationary state.

We investigated the influence of the channel density on the initial pulse amplitude, which we define as the top value (V_{top}) minus the stationary value (V_{eq}). In this way, the pulse height is also well defined when it is followed by sustained oscillations, and the growth of the amplitude at large stimulations is reduced as V_{top} and V_{eq} grow in similar manners. It should be mentioned that the pulse amplitude depends on the initial state, which is well separated from possible stationary states.

Fig. 7 shows the pulse amplitude for different channel density combinations, representing different points and

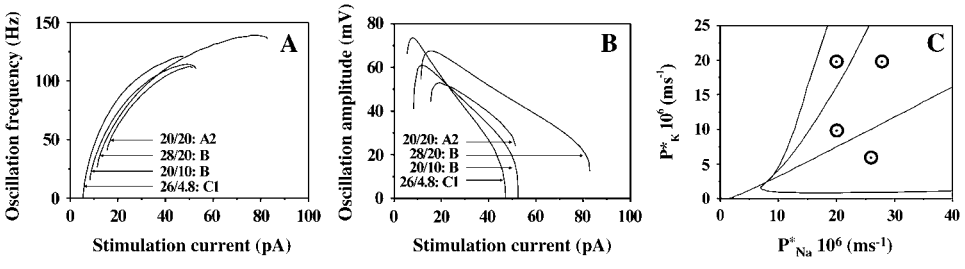

FIGURE 6 Encoding functions for the model neuron. Oscillation frequency (*A*) and steady-state impulse amplitude (*B*) dependence on stimulation and channel densities (P^*_{Na}/P^*_K pairs). (*C*) The location of the illustrated cases in the P^*_{Na}-P^*_K plane, demonstrating that all oscillatory subregions are represented (see Fig. 5). The curves are denoted by associated P^*_{Na}/P^*_K values in the dimension of 10^{-6} m s^{-1}. Also indicated are the oscillatory subregions of the P^*_{Na}/P^*_K pairs.

regions in the P^*_{Na}-P^*_K plane. Fig. 7 *A* shows the effect of varying the K channel density while keeping the Na channel density constant. It is clear that changed K channel densities do not change the curve shape significantly. Fig. 7 *B* shows a corresponding example where the Na channel density varies and the K channel density is kept constant. Clearly, more dramatic differences are evident here. Changing the Na channel density means shifting the activity of the model neuron from conditions where the amplitude is very sensitive to stimulation intensity (at low Na channel densities) to conditions of much less sensitivity (at high densities), even of insensitivity, i.e., all-or-nothing behavior.

Closer inspection also reveals that pulse amplitudes for channel density combinations in the C1 and C2 regions (curves 20/0.24, 20/3, and 20/6 in Fig. 7 *A*) show an abrupt, discontinuous start (i.e., a strict threshold in a mathematical sense), whereas those for channel density combinations in the B, A1, and A2 regions (curves 20/10, 10/10, 3/10, and 1.3/10 in Fig. 7 *B*) show a continuous growth, the steepness decreasing with decreasing P^*_{Na}.

With these kinds of results as a starting point, we can analyze features such as amplitude gradedness and all-or-nothing behavior. There are two relevant parameters to take into account: the existence of a proper threshold and the sensitivity of the amplitude to stimulus. These two features are not necessarily correlated. Fig. 7 *A* clearly shows that a variation of P^*_K does not imply great qualitative changes besides the discontinuous/very steep features discussed above, although the curves represent different regions in the P^*_{Na}-P^*_K plane with different oscillation properties (i.e., from the nonoscillation region C2 through oscillation regions C1, B, and A2).

Quantification of the gradedness

The lower curves in Fig. 7 *B* represent neuron models with a high sensitivity to stimulation not compatible with all-or-nothing behavior. In theory, such stimulation-sensitive behavior opens up for amplitude-coded information transfer between neurons. The sensitivity of the pulse amplitude to stimulation can be quantified in many ways. Here, we have chosen a measure which is equal to the stimulus range at which the derivatives (slopes) of the amplitude-stimulation curves (see Fig. 7, *A* and *B*) are larger than 0.25 mV/pA. Also, to avoid situations with very small pulses (in particular at the onsets of the curves), we exclude the ranges where pulse amplitudes are smaller than 1 mV. The gradedness measures thus obtained, plotted in the P^*_{Na}-P^*_K plane, are shown in Fig. 8.

As mentioned, there are other ways to define a gradedness measure, but the main features of Fig. 8, with large values (high sensitivity) to the left and small (low sensitivity or all-or-nothing-like behavior) to the right in the diagram, should be the same. It should be noted that the values go to zero for small (nonzero) values of P^*_{Na}. Pulses appear also when $P^*_{Na} = 0$, due to the activation of a K current (and thus do not represent real action potentials). They will, however, not be included as the slope of the corresponding amplitude-stimulation plots are too small. If we had chosen a lower value of the minimum slope (e.g., 0.1 mV/pA), most of the curves of Fig. 8 would be similar, but they would also include the P^*_K axis where $P^*_{Na} = 0$.

Fig. 8 confirms the view that strongly graded behavior is confined to regions that show no oscillatory behavior and all-or-nothing-like behavior to regions showing oscillatory activity. This is demonstrated in the figure where the dotted contours show the onset bifurcation subregions with the cases of Fig. 1 plotted (highly graded and all-or-nothing impulses outside the oscillatory regions and medium graded impulses in C1). The results suggest that neurons can switch between the two principal modes of information processing by regulating the number of active channels. Whether this occurs in reality remains to be discovered. The pharmacological importance of this suggestion is clearer: anesthetics block channels selectively (see Hutcheon and Yarom (1) and Hille (3)) and are expected to change the firing behavior, in some cases drastically.

DISCUSSION

This analysis shows that modifying the channel density causes the neuron model not only to change its firing from a nonspiking mode to a spiking one but to switch between qualitatively different firing patterns. At least three distinct oscillatory patterns, characterized by onset firing patterns of double-orbit, Hopf, and saddle-node type, can be distinguished.

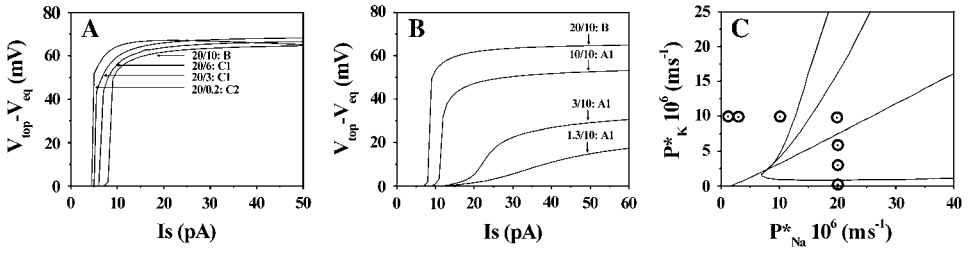

FIGURE 7 Impulse amplitude-stimulus diagrams showing the amplitude sensitivity to stimulation of the model neuron. Changed K channel density and constant Na channel density (*A*), and changed Na channel densities and constant K channel density (*B*). (*C*) The location of the illustrated cases in the P^*_{Na}-P^*_K plane (see Fig. 5). The curves are denoted by associated P^*_{Na}/P^*_K values in the dimension of 10^{-6} m s^{-1}. Also indicated are the oscillatory subregions in the P^*_{Na}-P^*_K plane.

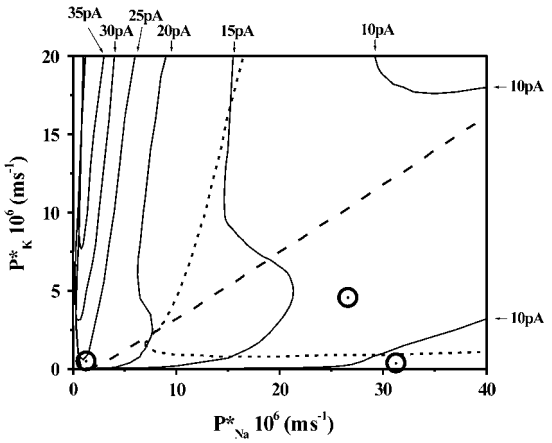

FIGURE 8 Pulse amplitude sensitivity to stimulation plotted in the channel density plane (P^*_{Na}-P^*_K). Sensitivity given as the range of stimulation current at which the current derivative of the impulse peak exceeds 0.25 mV pA^{-1} as described in the text. The numbers marking the contours are range values in pA. High stimulus sensitivity, i.e., a strongly graded impulse, is reflected in a high range value. The dotted line indicates the oscillatory region, shown in Fig. 5. The circles denote the locations of the cases in Fig. 1; the strongly graded case to the left, the all-or-nothing-like case to the (*lower*) right, and the medium graded/repetitive firing case in between (*upper right*).

The three oscillatory patterns are associated with three distinct areas in the channel density plane: the double-orbit pattern with area A1, the Hopf pattern with area B, and the saddle-node pattern with area C1. In contrast, the action potential amplitude sensitivity on stimulation changes continuously with channel density, the lowest sensitivity (all-or-nothing behavior) region overlying part of the saddle-node pattern region C1. This region roughly coincides with the oscillatory regions at low stimulation strengths (~5 pA region in Fig. 3).

Qualitatively similar results are obtained for other neuron models of the Hodgkin-Huxley type. However, the location of the oscillatory subregions in the density plane varies. Applying Na and K channel density data from the classical squid axon model of Hodgkin and Huxley (16) (after converting the conductance values to permeability values) and from the myelinated axon model of Frankenhaeuser and Huxley (15) to the hippocampal model here, we obtain values that place them in the oscillatory subregion C (saddle-node dynamics) of the P^*_{Na}-P^*_K plane. Nevertheless, both models show Hopf-type threshold dynamics, demonstrating the importance of also taking the passive membrane properties into account when constructing oscillatory maps for a neuron model.

Pharmacological modifications of oscillatory patterns

An increasing number of studies (4) show that channels are spontaneously and selectively up- and downregulated to adapt the activity of the parent neuron to a changing environment. This means that if these results apply to real neurons, their oscillatory activity and threshold dynamics can change during normal activity. Likewise, neurons can in theory switch between amplitude and rate coding behavior under physiological conditions. Similar changes in firing behavior can be achieved by a selective block of ion channels. Thus a selective block of K channels could switch a neuron with Hopf threshold dynamics (region B) and with a relatively high minimum frequency to saddle-node dynamics (region C1) with no low frequency limit. These findings suggest novel ways to interpret mechanisms of general anesthesia and novel strategies for constructing general anesthetics. An attractive idea would be that some anesthetics selectively block specific voltage-gated K channels in critical neurons, thereby contributing to the hypnosis effect. This idea does not seem far fetched: specific blocks of certain Kv channels have been reported for some general anesthetics (1,20). We have also shown (in voltage-clamp experiments with the oocyte preparation; 21) that some intravenous anesthetics specifically block Kv2.1 channels (22).

Saddle-node and Hopf-bifurcation dynamics in real neurons

These calculations were made for a neuron model comprising only two voltage-gated channel types. Furthermore, the calculation procedure in itself implies the assumptions of homogenously distributed channel populations and no interference by currents due to a complex dendritic morphology. How does this simplistic model apply to real neurons? This is so far little studied. However, both saddle-node (region C1) and Hopf-like (regions B and A2) threshold dynamics have been demonstrated in real neurons. They seem represented already in the classical study of *Carcinus maenas* axons (12), with class 1 axons displaying saddle node and class 2 axons displaying Hopf dynamics. Studies of cortical neurons also reveal similar types of threshold dynamics (13), with regular spiking neurons (often pyramidal cells) displaying saddle node type and fast spiking neurons (often interneurons) Hopf dynamics. Fig. 9 *A* shows recordings from mouse hippocampus mossy cells, demonstrating low frequency nondamped oscillations at threshold, resembling saddle-node dynamics. This study also suggests that transitions between different dynamics regimes should be possible. To date, few such transitions have been reported (but see Safronov et al. (19) showing transitions from damped to steady oscillations when Na channels in rat dorsal root neurons are recovering from TTX block, suggesting Hopf dynamics). In conclusion, this study adds another possible explanation to the variability of the oscillatory patterns in neurons at constant stimulation—an explanation complementing the hypotheses based on the dendritic structure (2) and the ion channel mixture (3,23).

Channel densities in neurons

How do the channel densities used in the calculations above relate to channel densities in real neurons? Some estimations

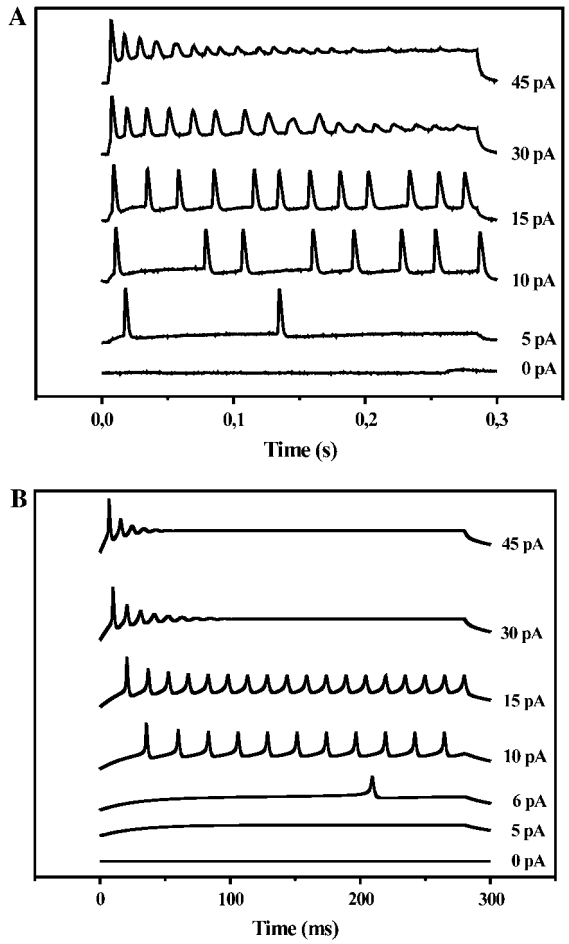

FIGURE 9 Saddle-node bifurcation behavior in a hippocampal interneuron. (*A*) Recordings from a mossy cell in the dentate gyrus with patch-clamp technique (whole-cell configuration). Stimulation current 5, 10, 20, 30 pA. Experimental details are given in (46). (*B*) Computed activity of the model neuron at channel densities $P^*_{Na} = 14 \times 10^{-6}$ and $P^*_K = 2 \times 10^{-6}$ m s^{-1}, located in region C1 (saddle-node bifurcation region) for stimulation currents 5, 10, and 15 pA.

of the distribution and density of channels in neurons collected from a fragmented literature are listed in Table 4. The trend is clear: the densities are very different in soma, initial segment, and axon. Thus, in mammalian neurons, the density of Na channels in soma and axon hillock is estimated to be low (1–5 channels per μm^2), whereas it is 100- to 200-fold higher in the initial segment and 1000-fold higher in the nodes of Ranvier (Table 4). The K channels form a more heterogeneous subfamily, and the densities are consequently even more difficult to quantify. Delayed rectifiers show low density in the soma (0.5–5 channels per μm^2) increases to a 50-fold higher density in the initial segment but decreases to almost zero density in the nodes of Ranvier. Recently, several investigations have challenged these estimations (24), suggesting a more homogenous distribution. Another controversial issue is the location of the triggering zone. Traditionally, the axon hillock and the initial segment have been assumed to serve this role. A number of studies suggest that the axon comprises the triggering zone (24,25). Assuming that the initial segment regulates the firing and that the higher density estimates are valid, we obtain a trigger critical density of 100–200 Na channels per μm^2 and 50 delayed rectifier K channels per μm^2. Since the original hippocampal neuron model is based on measurements from the soma of a hippocampal interneuron with a Na channel density of 5 channels per μm^2 and a delayed rectifier K channel density of 2.5 channels per μm^2 (calculated from data in Johansson and Arhem (8)), the Na channel density in the initial segment (150 channels per μm^2) corresponds to a 30-fold higher density than the original model density and the K channels in the initial segment (25 channels per μm^2) to a 10-fold higher density. Such a neuron would in our oscillation map be classified as a C1 or saddle-node neuron. Interestingly, the hippocampal mossy cells were also found to display saddle-node behavior (Fig. 9). We conclude that the densities discussed in this analysis are well within the physiological density range. Assuming lower densities of the initial segment, but also that the axon is the triggering zone, will not change these conclusions markedly. A discussion on the effects of spontaneous and pharmacological modifications of the densities and consequent impulse pattern changes therefore seems highly relevant.

TABLE 4 Channel densities (μm^{-2}), estimated from reported measurements

Na channels		
Soma		
Rat hippocampal interneuron	5	(8)
Rat pyramidal cell	5	(30)
Rat dorsal horn neuron	1	(19)
Initial segment		
Rat dorsal horn neuron	160	(31)
Axon		
Squid giant axon	339	(32)
Frog sciatic axon	920–1900	(33–36)
Rat sciatic axon	700–2000	(37,38)
Rat unmyelinated axon	200	(39)
K channels (delayed rectifiers)		
Soma		
Rat hippocampal interneuron	2.5	(8)
Rat pyramidal cell	5	(40)
Rat dorsal horn	0.5	(19)
Initial segment		
Rat dorsal horn neuron	25	(20)
Axon		
Squid giant axon	18–72	(32,41)
Frog sciatic axon	240–1100	(42–44)
Rat sciatic axon	0	(45)

Role of oscillatory pattern transitions for network behavior

How the natural and pharmacological modifications of neuronal firing behavior discussed above affect the global oscillatory activity is a cross-scale problem of extreme

complexity. The role of the many determining factors, the network configuration, the connectivity type, and strength and the intrinsic neuronal resonance, is still only fragmentarily understood. This analysis introduces the density of voltage-gated channels as another factor, contributing to the sculpturing of global oscillatory patterns.

We hypothesized above that neurons could switch from rate code to amplitude code information processing. For amplitude coding to play a role in the nervous system, the amplitude-modulated impulse, elicited in the trigger zone, should be able to propagate as modulated (i.e., with decreased amplitude) along the axon and into the terminals. This in turn depends on channel density and length factors of the axon and terminals. Low density (i.e., electrically passive) axons should not be so long that the impulse is eliminated by the electronic decrease; high density axons should not be so long that the initial downgraded impulse reaches full amplitude. This means that the main candidates for being rate-code/amplitude-code switcher neurons are interneurons with short axons.

The novel idea of obtaining general anesthetic effects by selectively blocking K channels is based on the proposal that human brain neurons firing in the γ-frequency range are involved in conscious activities, whereas lower frequencies characterize unconscious states such as sleep and general anesthesia (26–28). Shifting critical neurons from the B region (and high minimum frequency) to the C1 region (and lower minimum frequency) might cause global networks of the brain to switch from high to low frequencies (29) and the brain to switch from conscious to unconscious states.

APPENDIX: DETERMINING THE STABILITY OF THE STATIONARY SOLUTIONS

Below, we analyze the stationary states and stability features of the basic equations, Eqs. 1–4, here rewritten as

$$\begin{aligned} dv/dt &= I(v,m,h,n)/C_{\mathrm{M}} \\ &= (I_{\mathrm{S}} - I_{\mathrm{Na}}(v,m,h) - I_{\mathrm{K}}(v,n) - I_{\mathrm{L}}(v))/C_{\mathrm{M}} \end{aligned} \tag{A1}$$

$$dm/dt = \alpha_{\mathrm{m}}(v)\times(1-m) - \beta_{\mathrm{m}}m \tag{A2}$$

$$dh/dt = \alpha_{\mathrm{h}}(v)\times(1-h) - \beta_{\mathrm{h}}h \tag{A3}$$

$$dn/dt = \alpha_{\mathrm{n}}(v)\times(1-n) - \beta_{\mathrm{n}}n. \tag{A4}$$

In accordance with previous notations, we write $j = m$, h, or n. The time derivatives of these variables are zero when they are particular functions of the potential v as shown in Eq. 16, which we here rewrite

$$j_{\mathrm{stationary}} = j_\infty(v) = \alpha_{\mathrm{j}}(v)/[\alpha_{\mathrm{j}}(v) + \beta_{\mathrm{j}}(v)]. \tag{A5}$$

Equation 18, again rewritten here, then gives the stationary potential

$$I_\infty(v) = I(v, m_\infty(v), h_\infty(v), n_\infty(v)) = 0. \tag{A6}$$

The solution is $v = v0$, and we introduce notations for stationary m-, h-, n-values:

$$j0 = j_\infty(v0), j = m, h, \text{ or } n. \tag{A7}$$

Further, we extend the notations and write

$$j_1 = m, \quad j_2 = h, \quad j_3 = n. \tag{A8}$$

The next step is to investigate the differential equation solutions close to the stationary state. This is made in a conventional way. We replace the right hand sides by linear expressions and get the following equations (Note: $k = 1,2,3$; $j = m$, h, n. We have a double index notation and write, for instance, α_{jk}, which shall be interpreted by Eq. A8. Thus, as $j_1 = m$, $\alpha_{\mathrm{j1}} = \alpha_{\mathrm{m}}$, and other components similarly):

$$\begin{aligned} \frac{dv}{dt} &= JM_{0,0}\times(v - v0) + \sum_{\mathrm{k}=1}^{3} JM_{0,\mathrm{k}}\times(j_{\mathrm{k}} - j_{\mathrm{k}}0) \\ \frac{dj_{\mathrm{k}}}{dt} &= JM_{\mathrm{k},0}\times(v - v0) + JM_{\mathrm{k,k}}\times(j_{\mathrm{k}} - j_{\mathrm{k}}0). \end{aligned} \tag{A9}$$

The JM-elements are

$$\begin{aligned} JM_{0,0} &= \frac{\partial I(v,m0,h0,n0)/C_{\mathrm{M}}}{\partial j_{\mathrm{k}}}\Big|_{\mathrm{v=v0}} \\ JM_{0,\mathrm{k}} &= \frac{\partial I(v,n,h,m)/C_{\mathrm{M}}}{\partial j_{\mathrm{k}}}\Big|_{\mathrm{v=v0,n=n0,h=h0,n=n0}}, \end{aligned}$$

and (A10)

$$\begin{aligned} JM_{\mathrm{k}0} &= (\alpha'_{\mathrm{jk}}(v)\times\beta_{\mathrm{jk}}(v) - \alpha_{\mathrm{jk}}(v)\times\beta'_{\mathrm{jk}}(v)/(\alpha_{\mathrm{jk}}(v) + \beta_{\mathrm{jk}}(v)) \\ JM_{\mathrm{kk}} &= \alpha_{\mathrm{jk}} + \beta_{\mathrm{jk}}. \end{aligned}$$

The JM-functions are elements of a matrix:

$$\begin{pmatrix} JM_{00} & JM_{01} & JM_{02} & JM_{03} \\ JM_{10} & JM_{11} & 0 & 0 \\ JM_{20} & 0 & JM_{22} & 0 \\ JM_{30} & 0 & 0 & JM_{33} \end{pmatrix}$$

All elements are functions of the stationary potential $v0$. The elements of the upper row, but not the other ones, also contain the P*-parameters.

The (four) eigenvalues of this matrix are of principal relevance for determining the stability of the stationary states. These are obtained by standard methods and given as roots of a fourth order equation:

$$r^4 - A_3r^3 + A_2r^2 - A_1r + A_0 = 0. \tag{A11}$$

The A coefficients can be expressed as sums of products of the JM elements. A_3 is the sum of the diagonal elements (JM_{ii}), and A_0 is equal to the determinant. A_2 is a sum of products of two JM elements, and A_1 is a sum of products of three elements from different rows and columns.

Table 5 summarizes the cases discussed in this investigation. Two eigenvalues are always real and negative. The other two are the important ones in our analysis. In some cases both are real and one is positive, whereas the other is negative, yielding saddle-point dynamics. For most relevant situations, however, they are complex and their real parts can be positive or negative. The border situation when two eigenvalues are purely imaginary is particularly important, yielding a Hopf-bifurcation behavior. The condition for this can be expressed by demanding that a certain function P is equal to zero:

$$P = A_1^2 - A_1A_2A_3 + A_3^2A_0 = 0. \tag{A12}$$

This condition is derived from the relations between the roots and the coefficients in Eq. A11:

$$\begin{aligned} A_3 &= r_1 + r_2 + r_3 + r_4; \quad A_2 = (r_1 + r_2)(r_3 + r_4) + r_1r_2 + r_3r_4 \\ A_1 &= r_1r_2(r_3 + r_4) + (r_1 + r_2)r_3r_4; \quad A_0 = r_1r_2r_3r_4. \end{aligned}$$

If roots r_1 and r_2 are imaginary and r_3 and r_4 are real and negative, we can write

TABLE 5 Stability of stationary points and its relation to the eigenvectors of the linearization matrix *JM* (Eq. A11)

Character	r_1	r_2	r_3	r_4
Stable	Re < 0	Re < 0	Re < 0	Re < 0
			Im $= 0$	Im $= 0$
Saddle point	Re > 0	Re < 0	Re < 0	Re < 0
	Im $= 0$	Im $= 0$	Im $= 0$	Im $= 0$
Node	Re < 0	Re < 0	Re < 0	Re < 0
	Im $= 0$	Im $= 0$	Im $= 0$	Im $= 0$
Hopf-bifurcation	Re $= 0$	Re $= 0$	Re < 0	Re < 0
	Im $= +t$	Im $= +t$	Im $= 0$	Im $= 0$
Unstable	Re > 0	Re > 0	Re > 0	Re > 0
			Im $= 0$	Im $= 0$

A saddle node bifurcation occurs when a saddle point and a node merge.

$$r_1 = it;\quad r_2 = -it \text{ yielding } r_1 + r_2 = 0 \quad \text{and} \quad r_1 r_2 = t^2$$
$$r_3 + r_4 = -p;\quad r_3 r_4 = q^2.$$

Then $A_3 = -p$, $A_2 = t^2 + q^2$, $A_1 = -pt^2$ and $A_0 = t^2 q^2$.

The expression for P follows when the three variables p, t, q are eliminated in the four relations.

As an example we here show typical numerical values associated with points closing in on an end Hopf-bifurcation (the situation when stimulations cease to elicit repetitive firing). We choose the following P^*-values in the C1 region: $P^*_{Na} = 13 \times 10^{-6}$ m/s and $P^*_K = 2.4 \times 10^6$ m/s. With the stimulation current $I_s = 15$ pA, we get the stationary potential $v0 = -30.0$ mV and the *JM* matrix (units as given by the main definitions):

$$\begin{pmatrix} -186 & 27440 & 161400 & -54430 \\ 37.2 & -1307 & 0 & 0 \\ -1.14 & 0 & -274 & 0 \\ 5.17 & 0 & 0 & -358 \end{pmatrix}$$

The resulting eigenvalues are $r_1,r_2 = 8.21 \pm 440i$, $r_3 = -1830$, and $r_4 = -311.5$ (s^{-1}). The A coefficients are $A_3 = -2125$ (s^{-1}), $A_2 = 7.285 \times 10^5$ (s^{-2}), $A_1 = -4.051 \times 10^8$ (s^{-3}), and $A_0 = 1.103 \times 10^{11}$ (s^{-4}). $P = 3.53 \times 10^{16}$ (s^{-4}). $P > 0$ as are the real parts of $r_{1,2}$, implying instability of the system.

Next, we consider the case of stimulation current $I_s = 20$ pA. Then $v0 = -29.1$ mV and the matrix is

$$\begin{pmatrix} -205 & 25200 & 192100 & -59900 \\ 38.5 & -1317 & 0 & 0 \\ -1.03 & 0 & -292 & 0 \\ 5.36 & 0 & 0 & -348 \end{pmatrix}$$

The resulting eigenvalues are $r_{1,2} = -16.9 \pm 500i$, $r_3 = -1813$, and $r_4 = -315$ (s^{-1}). The A coefficients are $A_3 = -2162$ (s^{-1}), $A_2 = 8.926 \times 10^5$ (s^{-2}), $A_1 = 5.508 \times 10^8$ (s^{-3}), $A_0 = 1.426 \times 10^{11}$ (s^{-4}). $P = -9.3 \times 10^{16}$ (s^{-4}). $P < 0$ as are the real parts of $r_{1,2}$ implying stability of the system.

The bifurcation occurs close to $I_s = 16.58$ pA with $v0 = -29.71$ mV. The matrix is

$$\begin{pmatrix} -192.3 & 26880 & 171500 & -56230 \\ 37.7 & -1310 & 0 & 0 \\ -1.10 & 0 & -280 & 0 \\ 5.24 & 0 & 0 & -354 \end{pmatrix}$$

The resulting eigenvalues are $r_{1,2} = -0.009 \pm 460i$, $r_3 = -1825$, and $r_4 = -312$ (s^{-1}). The A coefficients are $A_3 = -2137$ (s^{-1}), $A_2 = 7.817 \times 10^5$ (s^{-2}), $A_1 = 4.526 \times 10^8$ (s^{-3}), and $A_0 = 12{,}076 \times 10^{11}$ (s^{-4}). $P = -5 \times 10^{13}$ (s^{-4}). P is three orders of magnitude smaller than in the other cases calculated above, and the real part of $r_{1,2}$ is close to zero. Both these facts imply that we are close to a Hopf-bifurcation point, as also indicated by the fact that P is four orders of magnitude smaller than the terms in the P expression.

This work was supported by grants from the Swedish Medical Research Council, the Swedish Society of Medicine, the Swedish Society for Medical Research, and the KI foundation.

REFERENCES

1. Hutcheon, B., and Y. Yarom. 2000. Resonance, oscillation and the intrinsic frequency preferences of neurons. *Trends Neurosci.* 23: 216–222.
2. Mainen, Z. F., and T. J. Sejnowski. 1996. Influence of dendritic structure on firing pattern in model neocortical neurons. *Nature.* 382:363–366.
3. Hille, B. 2001. Ionic Channels in Excitable Membranes. Sinauer Associates, Sunderland, MA.
4. Marder, E., and A. A. Prinz. 2002. Modeling stability in neuron and network function: the role of activity in homeostasis. *Bioessays.* 24: 1145–1154.
5. Stemmler, M., and C. Koch. 1999. How voltage-dependent conductances can adapt to maximize the information encoded by neuronal firing rate. *Nat. Neurosci.* 2:521–527.
6. Franks, N. P., and W. R. Lieb. 1994. Molecular and cellular mechanisms of general anaesthesia. *Nature.* 367:607–614.
7. Arhem, P., G. Klement, and J. Nilsson. 2003. Mechanisms of anesthesia: towards integrating network, cellular, and molecular level modeling. *Neuropsychopharmacology.* 28(Suppl 1):40–47.
8. Johansson, S., and P. Arhem. 1992. Membrane currents in small cultured rat hippocampal neurons: a voltage-clamp study. *J. Physiol.* 445:141–156.
9. Johansson, S., and P. Arhem. 1992. Computed potential responses of small cultured rat hippocampal neurons. *J. Physiol.* 445:157–167.
10. Gotch, F. 1902. The submaximal electrical response of nerve to a single stimulus. *J. Physiol.* (*Lond.*). 28:395–416.
11. Cole, K. S., R. Guttman, and F. Bezanilla. 1970. Nerve membrane excitation without threshold. *Proc. Natl. Acad. Sci. USA.* 65:884–891.
12. Hodgkin, A. L. 1948. The local electric changes associated with repetitive action in a non-medullated axon. *J. Physiol.* (*Lond.*). 107: 165–181.
13. Tateno, T., A. Harsch, and H. P. Robinson. 2004. Threshold firing frequency-current relationships of neurons in rat somatosensory cortex: type 1 and type 2 dynamics. *J. Neurophysiol.* 92:2283–2294.
14. Melnick, I. V., S. F. Santos, and B. V. Safronov. 2004. Mechanism of spike frequency adaptation in substantia gelatinosa neurones of rat. *J. Physiol.* 559:383–395.
15. Frankenhaeuser, B., and A. F. Huxley. 1964. The action potential in the myelinated nerve fiber of Xenopus laevis as computed on the basis of voltage clamp data. *J. Physiol.* 171:302–315.
16. Hodgkin, A. L., and A. F. Huxley. 1952. A quantitative description of membrane current and its application to conduction and excitation in nerve. *J. Physiol.* 117:500–544.
17. Hodgkin, A. L., and B. Katz. 1949. The effect of temperature on the electrical activity of the giant axon of the squid. *J. Physiol.* 109:240–249.
18. Koch, C. 1999. Biophysics of Computation: Information Processing in Single Neurons. Oxford University Press, Oxford, UK.
19. Safronov, B. V., M. Wolff, and W. Vogel. 1997. Functional distribution of three types of Na+ channel on soma and processes of dorsal horn neurones of rat spinal cord. *J. Physiol.* 503:371–385.
20. Harris, T., M. Shahidullah, J. S. Ellingson, and M. Covarrubias. 2000. General anesthetic action at an internal protein site involving the S4–S5 cytoplasmic loop of a neuronal K(+) channel. *J. Biol. Chem.* 275:4928–4936.

21. Stühmer, W., M. Stocker, B. Sakmann, P. Seeburg, A. Baumann, A. Grupe, and O. Pongs. 1988. Potassium channels expressed from rat brain cDNA have delayed rectifier properties. *FEBS Lett*. 242:199–206.

22. Nilsson, J., M. Madeja, and P. Arhem. 2004. Selective block of Kv channels by general anesthetics. *Biophys. J*. 86:537A.

23. Connor, J. A., and C. F. Stevens. 1971. Prediction of repetitive firing behaviour from voltage clamp data on an isolated neurone soma. *J. Physiol*. 213:31–53.

24. Colbert, C. M., and E. Pan. 2002. Ion channel properties underlying axonal action potential initiation in pyramidal neurons. *Nat. Neurosci*. 5:533–538.

25. Edwards, C., and D. Ottoson. 1958. The site of impulse initiation in a nerve cell of a crustacean stretch receptor. *J. Physiol*. 143:138–148.

26. John, E. R., and L. S. Prichep. 2005. The anesthetic cascade: a theory of how anesthesia suppresses consciousness. *Anesthesiology*. 102: 447–471.

27. Engel, A. K., P. Fries, and W. Singer. 2001. Dynamic predictions: oscillations and synchrony in top-down processing. *Nat. Rev. Neurosci*. 2:704–716.

28. Crick, F., and C. Koch. 2003. A framework for consciousness. *Nat. Neurosci*. 6:119–126.

29. Halnes, G., H. Liljenstrom, and P. Arhem. 2004. Density dependent neurodynamics. *Presented at The 5th International Conference on Biological Physics (ICBP)—Structure and dynamics of biomolecules, Gothenburg*.

30. Colbert, C. M., and D. Johnston. 1996. Axonal action-potential initiation and Na+ channel densities in the soma and axon initial segment of subicular pyramidal neurons. *J. Neurosci*. 16:6676–6686.

31. Safronov, B. V. 1999. Spatial distribution of NA+ and K+ channels in spinal dorsal horn neurones: role of the soma, axon and dendrites in spike generation. *Prog. Neurobiol*. 59:217–241.

32. Conti, F., L. J. De Felice, and E. Wanke. 1975. Potassium and sodium ion current noise in the membrane of the squid giant axon. *J. Physiol*. 248:45–82.

33. Conti, F., B. Hille, B. Neumcke, W. Nonner, and R. Stampfli. 1976. Measurement of the conductance of the sodium channel from current fluctuations at the node of Ranvier. *J. Physiol*. 262:699–727.

34. Dodge, F. A., and B. Frankenhaeuser. 1958. Membrane currents in isolated frog nerve fibre under voltage clamp conditions. *J. Physiol*. 143:76–90.

35. Sigworth, F. J. 1980. The variance of sodium current fluctuations at the node of Ranvier. *J. Physiol*. 307:97–129.

36. Sigworth, F. J. 1980. The conductance of sodium channels under conditions of reduced current at the node of Ranvier. *J. Physiol*. 307:131–142.

37. Neumcke, B., and R. Stampfli. 1982. Sodium currents and sodium-current fluctuations in rat myelinated nerve fibres. *J. Physiol*. 329:163–184.

38. Vogel, W., and J. Schwartz. 1995. Voltage-clamp studies in axons: macroscopic and single channel currents. *In* The Axons. S. Waxman, J. Kocsic, and P. Stys, editors. Oxford University Press, London, UK. 257–280.

39. Pellegrino, R. G., P. S. Spencer, and J. M. Ritchie. 1984. Sodium channels in the axolemma of unmyelinated axons: a new estimate. *Brain Res*. 305:357–360.

40. Hoffman, D. A., J. C. Magee, C. M. Colbert, and D. Johnston. 1997. K+ channel regulation of signal propagation in dendrites of hippocampal pyramidal neurons. *Nature*. 387:869–875.

41. Conti, F., and E. Neher. 1980. Single channel recordings of K+ currents in squid axons. *Nature*. 285:140–143.

42. Frankenhaeuser, B. 1962. Potassium permeability in myelinated nerve fibres of Xenopus laevis. *J. Physiol*. 160:54–61.

43. Neumcke, B., W. Schwarz, and R. Stampfli. 1980. Differences between K channels in motor and sensory nerve fibres of the frog as revealed by fluctuation analysis. *Pflugers Arch*. 387:9–16.

44. Conti, F., B. Hille, and W. Nonner. 1984. Non-stationary fluctuations of the potassium conductance at the node of Ranvier of the frog. *J. Physiol*. 353:199–230.

45. Brismar, T. 1980. Potential clamp analysis of membrane currents in rat myelinated nerve fibres. *J. Physiol*. 298:171–184.

46. Petersson, S., A. S. Persson, J. E. Johansen, M. Ingvar, J. Nilsson, G. Klement, P. Arhem, M. Schalling, and C. Lavebratt. 2003. Truncation of the Shaker-like voltage-gated potassium channel, Kv1.1, causes megencephaly. *Eur. J. Neurosci*. 18:3231–3240.